

Article

Effect of Metal Dopant on the Performance of Ni@CeMeO₂ Embedded Catalysts (Me = Gd, Sm and Zr) for Dry Reforming of Methane

André L. A. Marinho^{1,2,3}, Raimundo C. Rabelo-Neto² , Florence Epron³ , Fabio S. Toniolo¹ ,
Fabio B. Noronha^{2,4,*} and Nicolas Bion^{3,*} 

¹ Chemical Engineering Program of COPPE/UFRJ, Federal University of Rio de Janeiro, P.O. Box 68502, Rio de Janeiro 21941-972, RJ, Brazil

² National Institute of Technology, Catalysis Division, Rio de Janeiro 20081-312, RJ, Brazil

³ Institut de Chimie des Milieux et Matériaux de Poitiers (IC2MP), CNRS, University of Poitiers, 86073 Poitiers, France

⁴ University of Lille, CNRS, Centrale Lille, ENSCL, Univ. Artois, UMR 8181—UCCS—Unité de Catalyse et Chimie du Solide, 59000 Lille, France

* Correspondence: fabio.bellot@int.gov.br (F.B.N.); nicolas.bion@univ-poitiers.fr (N.B.)

Abstract: Biogas upgrading by a catalytic process has been studied in order to obtain syngas using renewable source of methane. This work evaluates the influence of metal dopant (Gd, Sm, and Zr) on the CeO₂ structure for the dry reforming of methane over Ni nanoparticle embedded catalysts. The doping with Zr improved the thermal stability of the catalyst, leading to the formation of small Ni nanoparticles, while Ni metal sintering was observed for Ni@CeO₂, Ni@CeGdO₂, and Ni@SmO₂, according to in situ XRD under reduction conditions. The ceria reducibility was affected by the dopant nature, for which the addition of Zr caused distortions in the ceria lattice, promoting the diffusion of oxygen bulk to surface. The doping with Gd and Sm created oxygen vacancies by charge compensation, and the saturation of oxygen vacancies in the fresh samples decreased the degree of Ce reduction, according to TPR results. The larger Ni particles and poor redox behavior for Ni@CeGdO₂ and Ni@CeSmO₂ were responsible for the high carbon formation on these catalysts during the DRM reaction. The Ni@CeZrO₂ catalyst did not present coke formation because of smaller Ni crystallite size and higher ceria reducibility. Therefore, the control of Ni particle size and the high oxygen mobility in the Ni@CeZrO₂ catalyst inhibits carbon deposition and enhances the mechanism of carbon removal, promoting the catalyst stability.

Keywords: Ni-embedded; ceria; ceria-zirconia; Gd-doped ceria; Sm-doped ceria; oxygen storage capacity; oxygen isotopic exchange; methane dry reforming; biogas



Citation: Marinho, A.L.A.; Rabelo-Neto, R.C.; Epron, F.; Toniolo, F.S.; Noronha, F.B.; Bion, N. Effect of Metal Dopant on the Performance of Ni@CeMeO₂ Embedded Catalysts (Me = Gd, Sm and Zr) for Dry Reforming of Methane. *Methane* **2022**, *1*, 300–319. <https://doi.org/10.3390/methane1040023>

Academic Editors: Brian A. Rosen and Oz M. Gazit

Received: 18 August 2022

Accepted: 18 November 2022

Published: 28 November 2022

Publisher's Note: MDPI stays neutral with regard to jurisdictional claims in published maps and institutional affiliations.



Copyright: © 2022 by the authors. Licensee MDPI, Basel, Switzerland. This article is an open access article distributed under the terms and conditions of the Creative Commons Attribution (CC BY) license (<https://creativecommons.org/licenses/by/4.0/>).

1. Introduction

Energy from renewable sources has gained much more attention in recent years due to the environmental impacts caused by greenhouse gases emission from fossil fuel [1,2]. Among the renewable sources, biogas plays a key role in the development of technologies to replace CH₄ dependency from the natural gas. Biogas is produced from the anaerobic digestion of biomass and it is a renewable source of methane and carbon dioxide [3]. Nowadays, biogas is mainly upgraded to biomethane and incorporated into natural gas networks [2]. Alternatively, biogas may be used for the production of syngas and hydrogen through the dry reforming of methane (DRM) [4,5]. This is an interesting route due to the presence of CH₄ and CO₂ in the raw biogas, decreasing the number of pretreatment steps before the reformer. Furthermore, CH₄ and CO₂ are greenhouse gases turning the DRM process environmentally friendly.

DRM is an endothermic reaction that requires high temperature ($>800\text{ }^{\circ}\text{C}$), which favors catalyst deactivation by metal sintering and carbon deposition. Therefore, the design of a stable catalyst is the main challenge for the DRM.

In order to improve the resistance to metal sintering, many strategies were applied to improve the Ni dispersion and different methods of catalyst preparation have been investigated, such as evaporation-induced self-assembly, core-shell, and sol-gel, to limit the Ni crystallite growth [6–13]. Ma et al. recently demonstrated that the addition of La increased the Ni dispersion over Al_2O_3 support, avoiding the formation of NiAl_2O_4 species [13]. However, the TGA analysis already shows the formation of carbon after 10 h of reaction. Zhang et al. [12] studied the performance of a Ni@SiO_2 core-shell catalyst for DRM reaction. They observed the resistance to Ni sintering at $850\text{ }^{\circ}\text{C}$ for 24.5 h on stream. However, N_2 physisorption measurements revealed that the porous structure of silica shell collapsed during reduction and reforming, which was attributed to the instability of silica shell under the high reaction temperature, especially in the presence of produced steam at high temperatures. This has also been reported in other studies using core-shell catalysts [14,15]. The formation of carbon filaments inside the nanocavities was inhibited but amorphous and graphitic carbon were still formed. Charisiou et al. demonstrated the effect of temperature on the type of carbon species formed during DRM reaction [16]. Performing the reaction above $750\text{ }^{\circ}\text{C}$, the carbon formed presents high graphitization degree and it is more easily oxidized by the O species over the $\text{Ni/CeO}_2\text{-ZrO}_2$ catalyst surface.

Therefore, control of metal sintering alone is not sufficient to prevent the formation of carbon deposits on Ni-based catalysts with unreducible supports. Furthermore, the synthesis methods for core-shell materials reported in the literature are still limited, present difficulty to control core size and shell thickness, and lead to low yield and high-price reactants [17]. These works reveal the importance of developing more simple methods to prepare embedded materials.

Recently, Ni nanoparticles embedded in CeO_2 (Ni@CeO_2) were synthesized by the sol-gel method and compared with a Ni/CeO_2 prepared by support impregnation [6]. The performance of the catalysts was investigated in the DRM reaction. Ni embedded in CeO_2 improved the resistance to sintering along the reduction at $800\text{ }^{\circ}\text{C}$ and reduced the carbon formation rates during DRM reaction at $800\text{ }^{\circ}\text{C}$. These results were attributed to the higher metal-support interaction and larger amount of oxygen vacancies.

Ceria (CeO_2) has been extensively used as a support of catalysts for DRM reaction due to its redox properties [18–21]. Ceria has a very high oxygen exchange capacity since this oxide may reversibly change its oxidation states between Ce^{4+} and Ce^{3+} , resulting in the generation of oxygen vacancies [22]. Therefore, at DRM conditions, the carbon deposits can be gasified by lattice oxygen from CeO_2 and the CO_2 dissociates on oxygen vacancies, promoting the carbon removal mechanism [23,24]. The oxygen storage capacity (OSC) can be influenced by ceria surface area and particle size and by the addition of dopants into CeO_2 structure [25–28].

The addition of dopants promotes the OSC of ceria-based materials [20,28–31]. The most common dopant found in the literature is zirconia. The substitution of Zr^{4+} for Ce^{4+} generates oxygen vacancies due to the distortion of ceria lattice [6,32–34]. Zirconia also promotes thermal stability of ceria, avoiding the sintering at high temperature [6,35]. Doping of ceria with lower valence rare-earth elements, such as Gd^{3+} and Sm^{3+} , results in the formation of oxygen vacancy by charge compensation [28].

Luisetto et al. [20] studied the effect of Zr and Sm doped- CeO_2 over Ni/CeO_2 catalyst in the DRM reaction. They observed by Raman spectroscopy that the number of defects created by doping ceria with Sm was higher than that for Zr doping. Ni particle size was extremely affected by metal dopant, for which Ni/CeZrO_2 presented the smallest value (11 nm) against 37 nm for Ni/CeSmO_2 , indicating the low thermal stability of Sm-doped ceria materials.

The aim of the present work is to investigate, for catalysts constituted of Ni-embedded in ceria support, the effect of different metal dopants (Gd^{3+} , Sm^{3+} and Zr^{4+}) for limiting the carbon deposition. The effect of the type of dopant on the nature of oxygen vacancies (created by charge compensation or structural relaxation in the ceria structure) and on the rate of carbon formation during DRM reaction was evaluated. The reducibility and oxygen mobility of the catalysts were characterized by in-situ X-ray diffraction, temperature-programmed reduction, and isothermal oxygen isotopic exchange experiments. The latter characterization technique, not classically used for investigating DRM catalysts, is well suited to study the impact of dopants in the diffusion of O^{2-} from the ceria bulk to the surface where the carbon deposition occurs. The carbon deposits were measured by thermogravimetric analysis and scanning electron microscopy.

2. Results and Discussion

2.1. Catalyst Characterization

The chemical composition and surface area of the samples are reported in Table 1. The Ni content and Ce/dopant molar ratio are close to the nominal value (i.e., Ni wt.% = 10 and Ce/dopant molar ratio = 4.0). After reduction at 800 °C under pure H_2 , all catalysts exhibited very low surface area due to the low thermal stability of ceria at this high reduction temperature [22]. The addition of Gd or Sm to ceria did not change the thermal stability of the catalysts, which showed surface area lower than 10 m^2/g . Silva et al. [31] also did not observe in their work any changes in the surface area for Ni/CeGdO₂ compared to Ni/CeO₂. The addition of Zr slightly increased the thermal stability of the catalyst, presenting the highest surface area among them. Several works in the literature [35–37] also reported the beneficial effect of Zr to enhance CeO₂ thermal stability by the formation of a CeZrO₂ solid solution.

Table 1. Chemical composition and surface area after reduction at 800 °C of the catalysts.

Catalyst	Ni (wt%)	CeO ₂ (wt%)	Dopant (wt%)	Ce/Dopant Molar Ratio	Surface Area of Reduced Sample (m ² /g)
Ni@CeO ₂	9.7	87.2	—	—	<10
Ni@CeGdO ₂	9.8	72.1	15.1	4.2	<10
Ni@CeSmO ₂	9.7	72.4	17.9	4.1	<10
Ni@CeZrO ₂	9.5	74.4	13.4	4.0	20

Figure 1a shows the diffractograms of the fresh samples at room temperature. The XRD patterns were converted to $\text{CuK}\alpha$ radiation ($\lambda = 1.5406 \text{ \AA}$), for direct comparison with the literature. The line at $2\theta = 44.5^\circ$ is due to the Khantal-based support used in the in situ XRD equipment. The diffractogram of Ni@CeO₂ catalyst exhibited the characteristic lines of CeO₂ with fluorite-like structure (JCPDS 34-0394) at $2\theta = 28.46^\circ$, 32.92° , 47.39° , and 56.33° . These lines are marked with dashed lines to facilitate the discussion about the shifts observed with the addition of different dopants. The insertion of dopants shifts the main CeO₂ line to lower (Ni@CeGdO₂ = 28.37° , Ni@CeSmO₂ = 28.33°) or higher (Ni@CeZrO₂ = 28.79°) 2θ values (Figure 1b) as a consequence of expansion or contraction of the ceria lattice, respectively. The ceria lattice for the calcined samples was: Ni@CeO₂ (5.4237 Å); Ni@CeGdO₂ (5.4460 Å); Ni@CeSmO₂ (5.4565 Å); Ni@CeZrO₂ (5.3681 Å). The partial substitution of Ce^{4+} (0.97 Å) by cations with larger atomic radii, such as Gd^{3+} (1.16 Å) or Sm^{3+} (1.08 Å), causes an expansion in the ceria lattice [38]. The Zr^{4+} addition leads to a contraction of the ceria lattice since its atomic radius (0.84 Å) is smaller than that for Ce^{4+} (0.97 Å). In our work, the XRD of fresh samples reveals that Gd, Sm, and Zr partially substitute Ce^{4+} into the structure, leading to the formation of CeGdO₂, CeSmO₂, and CeZrO₂ solid solutions [32,39–41]. The lines characteristic of NiO were not detected in the diffractograms of the calcined samples, indicating the presence of highly dispersed particles, as observed in our previous work [6].

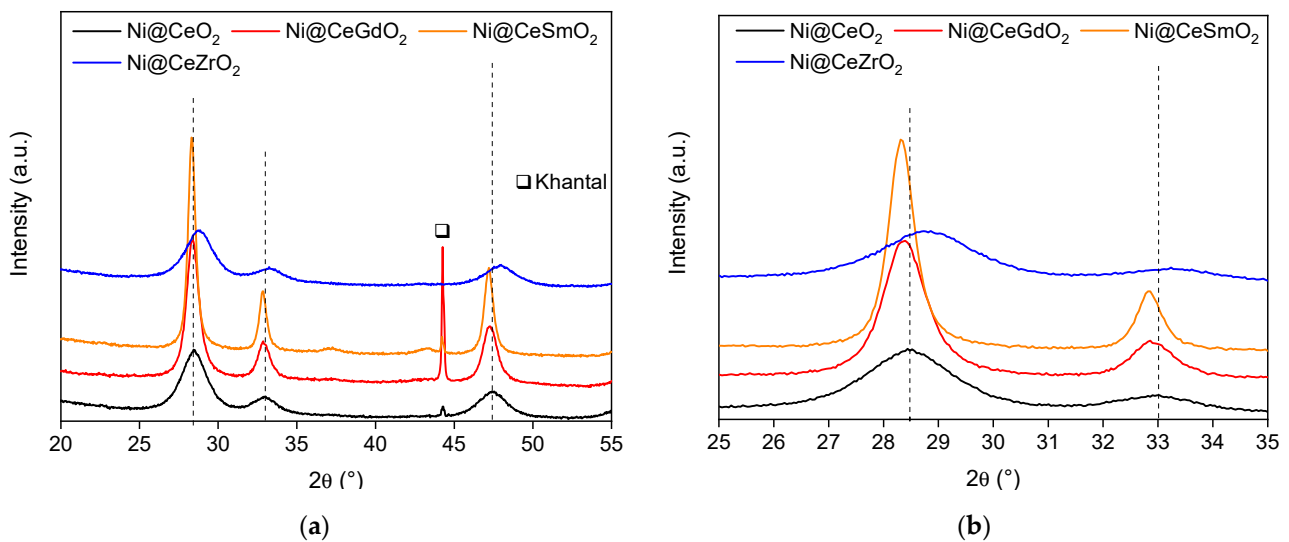


Figure 1. XRD patterns of fresh samples at room temperature: (a) $2\theta = 20\text{--}55^\circ$; (b) $2\theta = 25\text{--}35^\circ$.

In-situ diffractograms obtained during reduction of the samples are presented in Figure 2. For Ni@CeO₂, Ni@CeGdO₂, and Ni@CeSmO₂, the positions of the ceria lines remain unchanged during reduction up to 300 °C. Further heating up to 500 °C slightly shifts the diffraction lines to lower 2θ angles. Increasing the temperature up to 800 °C results in a significant shift of these lines. The shift of characteristic lines of ceria to lower 2θ angles during reduction of all samples could be due to: (i) the thermal expansion of the unit cell and/or; (ii) the reduction of Ce⁴⁺ to Ce³⁺, which has larger ionic radii (1.14 Å) [42]. Therefore, the shift on the ceria lines observed during the reduction process is a result of the balance between these two effects. On the other hand, for the Ni@CeZrO₂ catalyst, a shift in the ceria lines is observed when the sample is reduced at 300 °C, and this displacement increases when the sample is heated up to 800 °C. The formation of CeZrO₂ solid solution favors ceria reduction at lower temperature compared to Ce-doped with Gd or Sm.

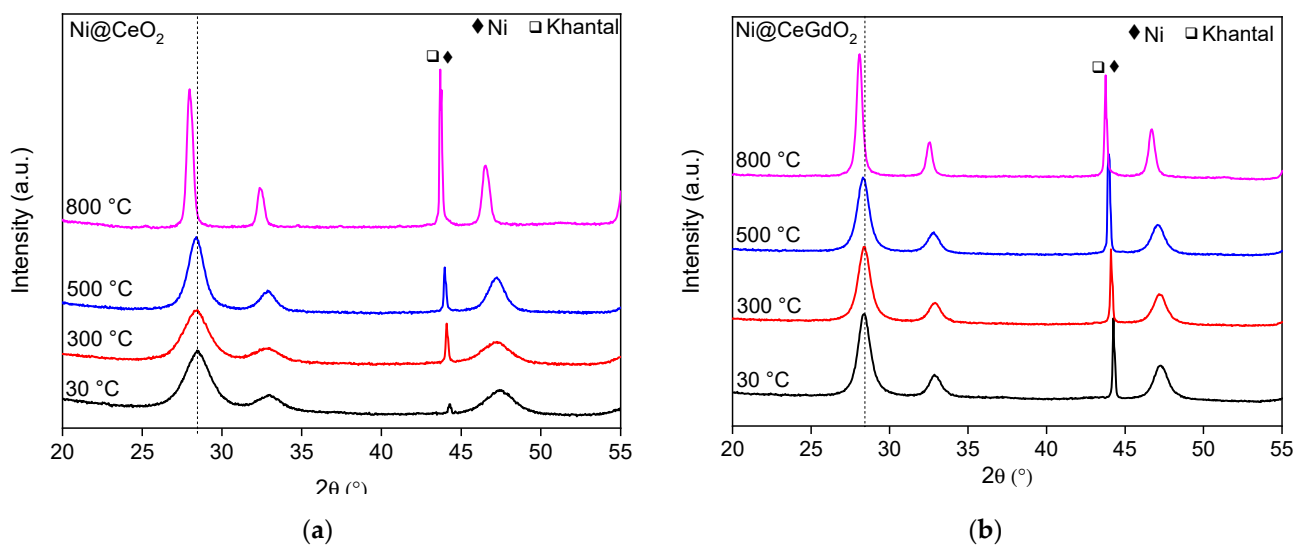


Figure 2. Cont.

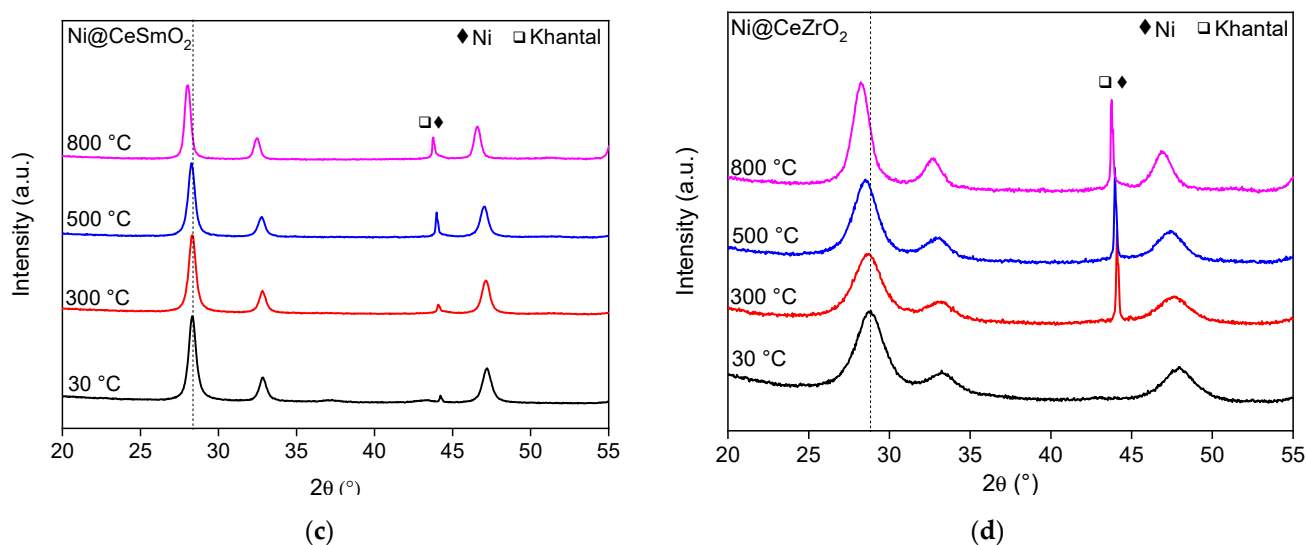


Figure 2. In-situ diffractograms obtained during reduction of (a) Ni@CeO₂, (b) Ni@CeGdO₂, (c) Ni@CeSmO₂ and (d) Ni@CeZrO₂.

In-situ XRD experiments under air of a NiO-CeO₂ physical mixture up to 800 °C (not shown) were carried out to evaluate the influence of the thermal expansion on the ceria lattice parameter. The thermal expansion was responsible for an increase in the CeO₂ lattice of 0.04 Å. Thus, a variation in this parameter higher than that value can be associated with the formation of Ce³⁺ by ceria reduction.

Figure 3a shows the variation of the calculated ceria lattice parameter as a function of reduction temperature for all catalysts. Increasing the temperature up to 800 °C, it is observed a slight increase in the ceria lattice parameter for Ni@CeO₂, Ni@CeGdO₂ and Ni@CeSmO₂ catalysts. However, the increase is much more important when the CeZrO₂ solid solution is formed. The ceria lattice expansion follows the order: Ni@CeGdO₂ (0.0556 Å) < Ni@CeSmO₂ (0.0656 Å) < Ni@CeO₂ (0.0924 Å) < Ni@CeZrO₂ (0.1011 Å). Therefore, the values of ceria lattice expansion were higher than 0.04 Å, indicating the formation of Ce³⁺ by ceria reduction for all catalysts. However, the reduction degree of ceria depends on the type of dopant. The XRD data suggest that the doping with Gd and Sm inhibits ceria reduction while the presence of Zr promotes the reduction of CeO₂.

Figure 3b shows the evolution of ceria crystallite size during reduction. The calcined samples doped with Gd and Sm exhibit the largest ceria crystallite size. Ni@CeO₂ and Ni@CeGdO₂ catalysts undergo a significant growth of the ceria crystallite size above 500 °C, but the sintering degree was more important for the undoped sample. For the samples doped with Sm and Zr, the ceria crystallite size only slightly increases during reduction at 800 °C. These results demonstrate that doping ceria increases the resistance to sintering during reduction at high temperature and this effect is more pronounced for Sm and Zr. Ni@CeZrO₂ exhibits the smallest ceria crystallite size after reduction at 800 °C. The high thermal stability of the Zr-doped ceria catalysts has been attributed to the CeZrO₂ solid solution formation [35,43,44].

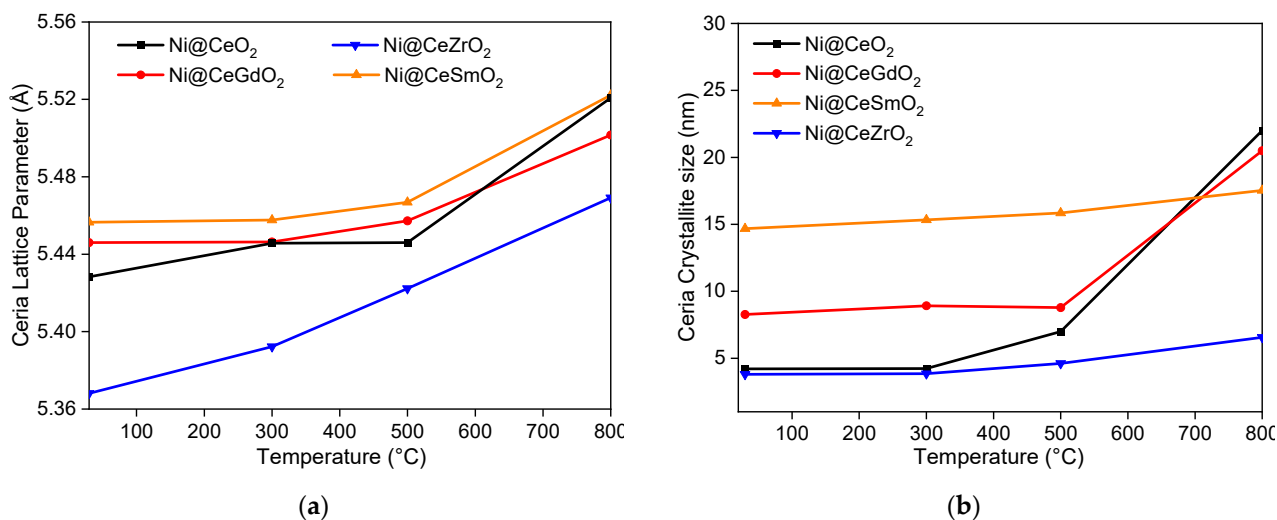


Figure 3. Variation of (a) ceria lattice parameter and (b) ceria crystallite size during reduction process.

Ni crystallite size was not calculated from the in situ diffractograms because the main characteristic line of metallic Ni is overlapped by Khantal line at $2\theta = 44.5^\circ$, and the (200) plane of Ni⁰ is characterized by a low intensity peak. Therefore, the Ni crystallite size was calculated by XRD after ex-situ reduction of the catalysts at 800 °C followed by passivation. The results are reported in Table 2. The Ni crystallite size is approximately the same for Ni@CeO₂, Ni@CeGdO₂, and Ni@CeSmO₂ (between 9.5 and 11.0 nm) while it is smaller for Zr-doped material (5.4 nm). The high resistance to CeO₂ sintering observed for Ce-doped with Zr catalysts avoids Ni sintering.

Table 2. Ni crystallite size calculated for the catalysts reduced at 800 °C followed by passivation and TOF values for the dry reforming of methane at 600 °C.

Catalyst	Ni Crystallite Size (nm)	TOF (s ⁻¹)
Ni@CeO ₂	10.7	3.6
Ni@CeGdO ₂	11.0	3.6
Ni@CeSmO ₂	9.5	3.7
Ni@CeZrO ₂	5.4	2.7

The Raman spectra of the calcined samples are shown in Figure 4. The sharp band at 460 cm⁻¹ is ascribed to the symmetrical stretching mode between the eight oxygen atoms bound to the cerium atom in the triple degenerate F_{2g} mode. The addition of different dopants slightly shifted the position of the band to higher Raman shift, due the modification of Ce-O force constant, evidencing the solid solution formation as previously demonstrated by XRD. Besides this intense band, it is possible to observe for all catalysts the presence of additional bands at 549 and 634 cm⁻¹ assigned to defect-induced mode. The comparison with a Ni/CeO₂ catalyst prepared by classical impregnation was already reported in a previous study [6], and eliminated the possibility that these bands were due the NiO vibration modes.

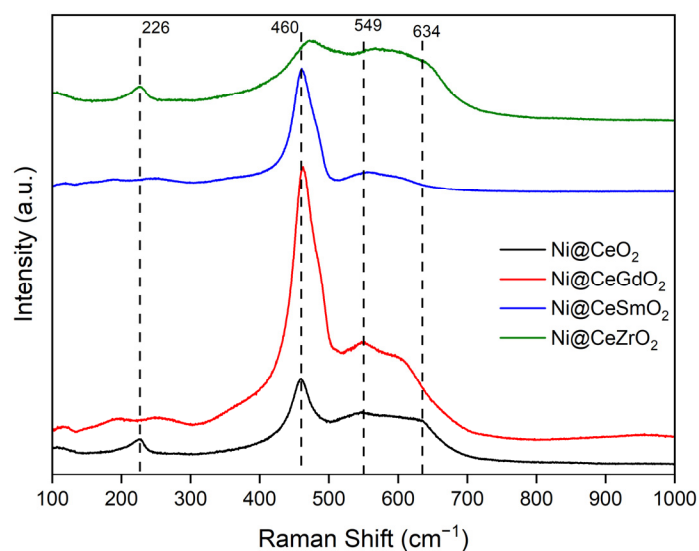


Figure 4. Raman spectra for the calcined samples.

Two different defects are reported in the literature: the Raman band at 549 cm^{-1} is associated to defect space including O^{2-} vacancy (O_v), while the band at 634 cm^{-1} is associated to defects space without O^{2-} vacancy [45,46]. Moreover, the Ni@CeO_2 and Ni@CeZrO_2 catalysts presented an additional band at 226 cm^{-1} assigned to second-order transverse acoustic mode (2TA). Among the catalysts, it is possible to observe that the F_{2g} band is much more intense for the catalysts doped with Gd and Sm. According to Loridant [47], the broadening observed in the Ni@CeO_2 and Ni@CeZrO_2 catalysts would be due to the presence of defects and to lower CeO_2 crystallite sizes observed for these catalysts. On the basis of the O_v/F_{2g} intensity ratio as proposed in [46], one can conclude that the degree of defects associated to oxygen vacancies increases with the following order $\text{Ni@CeGdO}_2 < \text{Ni@CeSmO}_2 < \text{Ni@CeO}_2 < \text{Ni@CeZrO}_2$.

TPR analysis was performed to study the reducibility of each catalyst and the profiles are shown in Figure 5. The TPR profile of Ni@CeO_2 catalyst exhibits broad peaks at low temperature (below $600\text{ }^\circ\text{C}$) and above $800\text{ }^\circ\text{C}$. Ni@CeGdO_2 and Ni@CeSmO_2 catalysts show two peaks at 340 and $420\text{ }^\circ\text{C}$, but the peak at high temperature is no longer observed. Ni@CeZrO_2 catalyst shows peaks at 340 and $420\text{ }^\circ\text{C}$ and a shoulder at $490\text{ }^\circ\text{C}$.

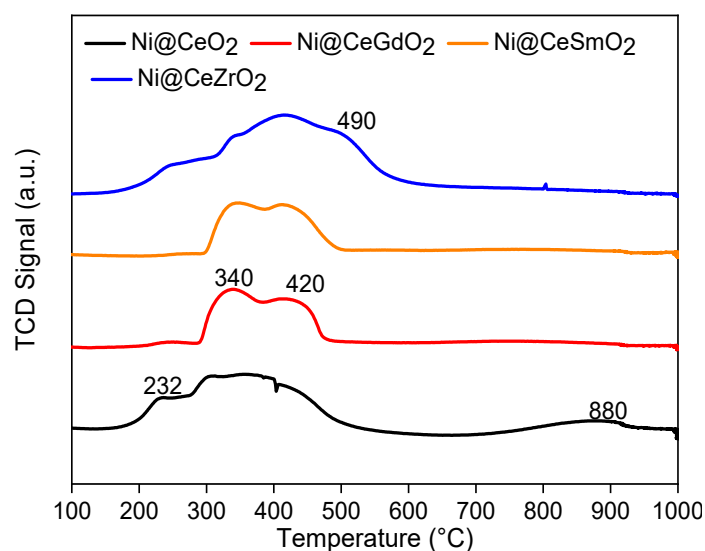


Figure 5. TPR profiles for the catalysts.

In situ XANES experiments at the Ni K-edge and Ce L_{III} edge were carried out to investigate the reduction of Ni/CeO₂ catalysts [6,48]. The XANES analyses at the Ni K-edge reveal that NiO is completely reduced up to 750 °C. The reduction of Ce⁴⁺ to Ce³⁺ occurs in two different regions: the low temperature region (200–650 °C), which is associated with the reduction of surface ceria; and the reduction of bulk ceria at high temperature (above 650 °C). Therefore, the reduction of NiO and surface CeO₂ occurs simultaneously at the low temperature region. Once the metallic Ni particles are formed, hydrogen is dissociated on the Ni surface and spills over to ceria, promoting its reduction. In our work, the peaks below 600 °C can be attributed to the simultaneous reduction of NiO and surface CeO₂, while the peak at high temperature observed in the TPR profile of Ni@CeO₂ corresponds to the reduction of bulk CeO₂.

Table 3 reports the H₂ uptake and the reduction degree of ceria calculated from the TPR profiles, considering the complete reduction of NiO. The reduction degree of ceria varied in the following order: Ni@CeGdO₂ (7%) < Ni@CeSmO₂ (13%) < Ni@CeO₂ (20%) < Ni@CeZrO₂ (35%). This trend is exactly the same observed for the ceria lattice expansion calculated from the in situ diffractograms during the reduction. Therefore, these results confirm that Gd and Sm-doped ceria catalysts exhibit lower ceria reducibility than undoped ceria. Hennings and Reimert [49] also demonstrated by TPR measurements that the doping of CeO₂ with different Gd contents reduced the degree of reduction of ceria.

Table 3. H₂ uptake and CeO₂ reduction degree calculated from TPR.

Catalyst	H ₂ Uptake (μmol/g)		Theoretical H ₂ Consumption for Total Reduction (μmol/g)		Ce ⁴⁺ /Ce ³⁺ Reduction (%)
	Low Temperature	High Temperature	Ni ²⁺ /Ni ⁰	Ce ⁴⁺ /Ce ³⁺	
Ni@CeO ₂	2022.7	643.3	1652.7	5066.4	20
Ni@CeGdO ₂	1963.0	—	1669.7	4190.1	7
Ni@CeSmO ₂	2199.7	—	1652.7	4207.5	13
Ni@CeZrO ₂	3131.4	—	1618.5	4322.7	35

The addition of Zr strongly increases the Ce⁴⁺ to Ce³⁺ reduction from 20% (on Ni@CeO₂) to 35% (on Ni@CeZrO₂). The higher reducibility of Zr-doped catalysts is due to the formation of ceria-zirconia solid solution, which has higher oxygen mobility [34]. The CeZrO₂ solid solution is described in the literature as a highly reducible material and it has been extensively used as catalyst support for DRM reaction [50–52]. Chen et al. [53] studied the Ni/Ce_{0.75}Zr_{0.25}O₂ catalyst for DRM reaction and they also observed a high H₂ consumption for CeZrO₂ materials compared to pure CeO₂. The doping with Zr promotes the mobility of oxygen from bulk to surface, enhancing the ceria reducibility.

The experiments of isotopic oxygen exchange were carried out at 400 °C and the results showing the evolution of the number of exchanged atoms (N_e) for the Ce-doped materials are depicted in Figure 6. The Ni@CeO₂ catalyst presents a continuous increase on N_e during the time exposed at ¹⁸O₂, reaching the value of 33 × 10²⁰ at·g^{−1} after 90 min.

Comparing the different dopants, Gd and Sm rapidly reach the equilibrium value at 400 °C, around N_e = 35 × 10²⁰ at·g^{−1}. The high rate of exchange obtained for these catalysts is due to the presence of high surface exchange activity. According to the literature [54,55], Gd and Sm segregate to the ceria surface and, therefore, the oxygen vacancies are more pronounced over the material surface, enriching the surface activity. In contrast, the Ni@CeZrO₂ catalyst presents a lower initial rate of exchange and slightly higher N_e after 2 h (37 × 10²⁰ at·g^{−1}) under ¹⁸O₂. The initial exchange rate, dependent on the concentration of surface sites able to activate the O₂ molecule, was not expected to be the lowest for this sample which exhibits the lowest crystallite size (highest specific surface area). This emphasizes the presence of preferential sites, e.g., oxygen vacancies for Gd and Sm-doped samples. On the contrary, the higher N_e value observed for the Ni@CeZrO₂ catalyst confirms the role of Zr substitution in ceria to favor the bulk diffusion.

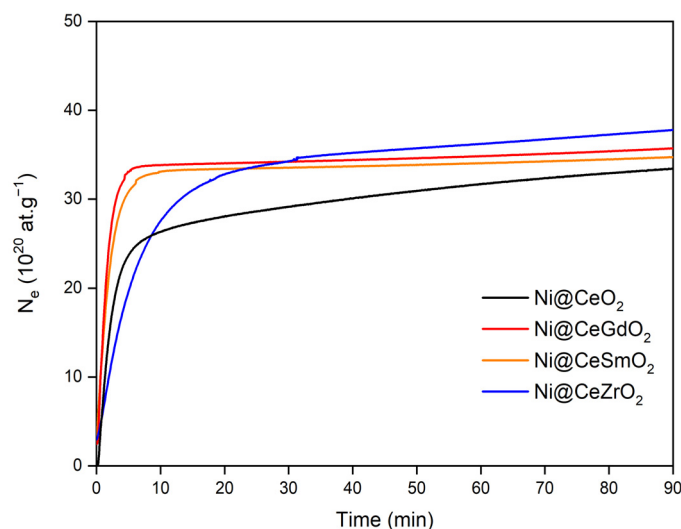


Figure 6. Evolution of the number of exchanged oxygen atoms during IOIE at 400 °C for Ni@CeO₂, Ni@CeGdO₂, Ni@CeSmO₂ and Ni@CeZrO₂.

Hennings and Reimert [49] observed that the total oxygen storage capacity (OSC) decreased with the increase in the Gd content in the ceria lattice. This result was attributed to the replacement of Ce⁴⁺ ions by non-reducible Gd³⁺ ions and the lower Ce⁴⁺ conversion.

Our experiments point out that the doped-catalysts present similar N_e, but the oxygen exchange dynamic depends on the dopant metal. Doping with Gd and Sm favors the exchange only at surface level, while doping with Zr favors the participation of bulk oxygen species, which will increase the number of oxygen vacancies under reaction condition.

2.2. DRM Reaction

Figure 7 displays the conversions of CO₂ and CH₄ expected at the thermodynamic equilibrium as a function of temperature. This analysis was performed by using the Gibbs free energy minimization algorithm on Aspen HYSYS Software assuming no carbon formation. At 800 °C, the conversions of 95 and 90% are reached at the equilibrium for CO₂ and CH₄ respectively. The highest conversion for CO₂ is explained by the occurrence of the reverse water-gas shift reaction (RWGS: CO₂ + H₂ → CO + H₂O) which is an endothermic reaction thermodynamically favored at high temperature, converting the CO₂ in CO in the presence H₂. This side reaction leads to a decrease of the H₂/CO molar ratio in the produced syngas.

Table 2 lists the initial turnover frequency (TOF) values of the catalysts for the DRM at 600 °C calculated at low CH₄ conversion. All catalysts exhibit approximately the same TOF values (between 2.7 and 3.7 s⁻¹), which is reasonable since they have the same Ni dispersion. TOF values obtained in our work are in agreement with those reported by Wei and Iglesia [56] for Ni/MgO (4.0 s⁻¹—Ni crystallite size = 6.7 nm).

The stability test was carried out to evaluate the resistance of the catalysts to carbon deposition during the DRM. The operating conditions were adapted in order to avoid reaching the thermodynamic equilibrium, allowing a relevant comparison in terms of catalyst deactivation. CH₄ and CO₂ conversions and H₂/CO molar ratio are shown as a function of time on stream (TOS) in Figures 8 and 9, respectively. CH₄ and CO₂ conversions remain quite constant during 24 h of TOS for all catalysts. The CO₂ conversion is higher than CH₄ conversion for all catalysts while the H₂/CO molar ratio is lower than 1.0. These results suggest the occurrence of the reverse water-gas shift (RWGS) reaction, which is thermodynamically favored at the reaction conditions used. A similar result was reported by other authors [32,41,57]. The Gd and Sm-doped catalysts present higher initial H₂/CO molar ratio, followed by Ni@CeO₂ and Ni@CeZrO₂.

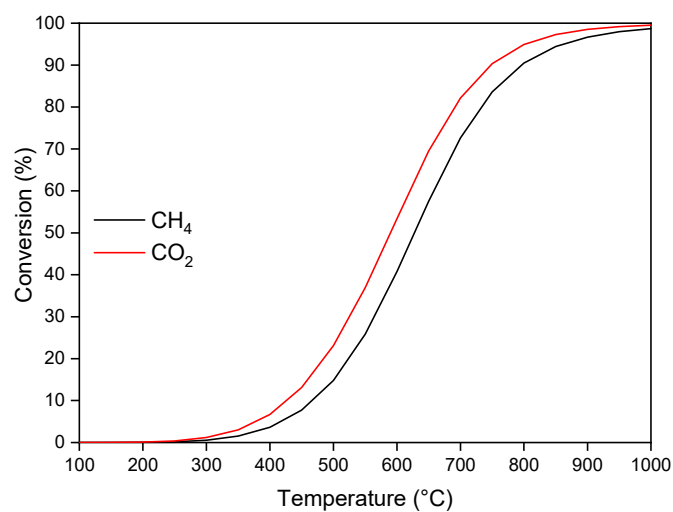


Figure 7. Reactant conversion and H_2/CO molar ratio at the thermodynamic equilibrium of the DRM reaction assuming no carbon formation.

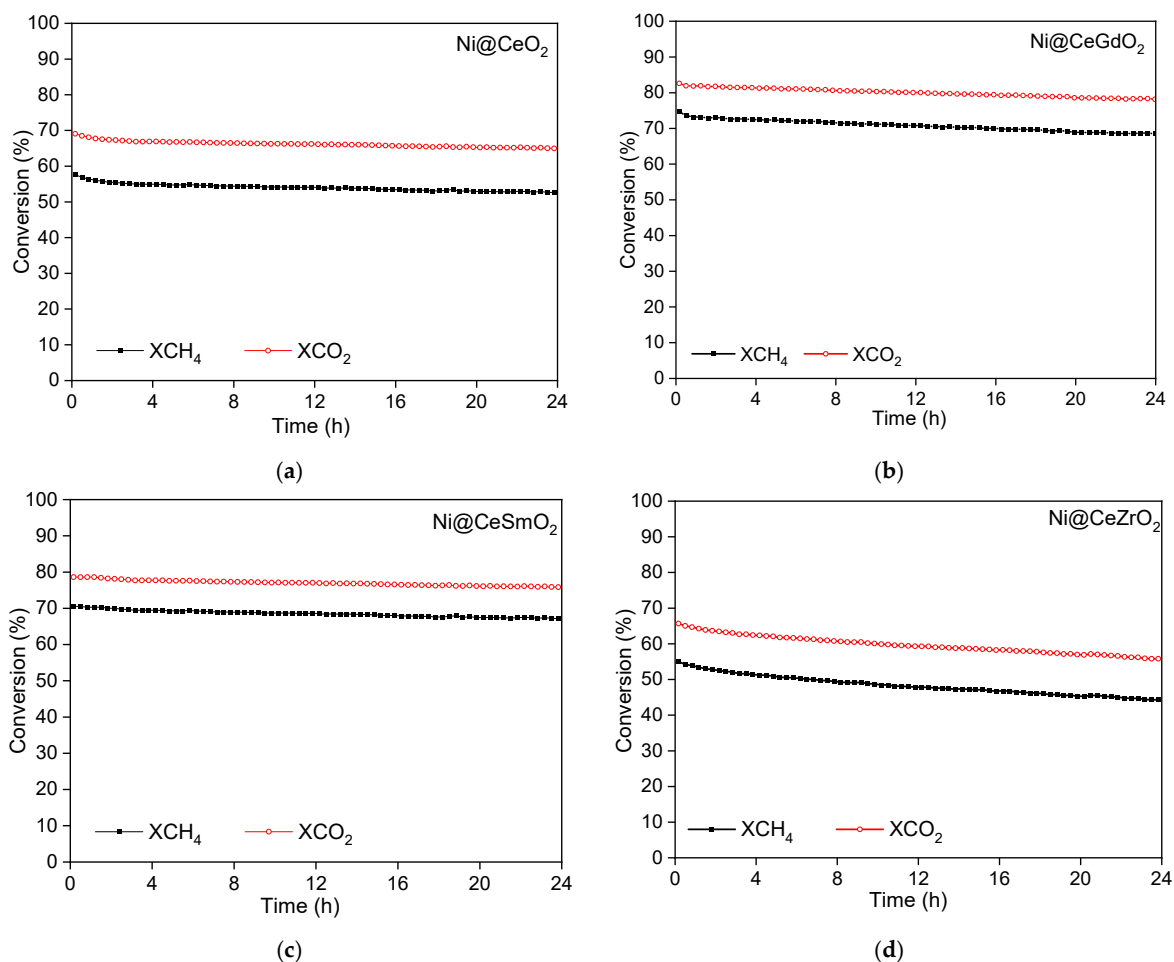


Figure 8. Conversion of CH_4 and CO_2 in the DRM at $800\text{ }^\circ\text{C}$ as a function of TOS (CH_4/CO_2 molar ratio of 1.0; $W/F = 0.2\text{ g}_{\text{cat}}\cdot\text{L}^{-1}\text{h}^{-1}$) for (a) $Ni@CeO_2$, (b) $Ni@CeGdO_2$, (c) $Ni@CeSmO_2$ and (d) $Ni@CeZrO_2$.

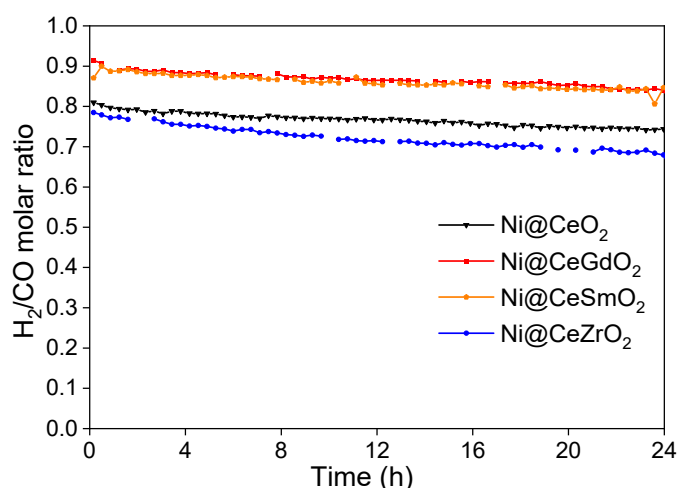


Figure 9. H₂/CO molar ratio obtained in the the DRM at 800 °C as a function of TOS (CH₄/CO₂ molar ratio of 1.0; W/F = 0.2 g_{cat}·L⁻¹h⁻¹).

2.3. Characterization of Spent Catalysts

After the stability test, the post-reaction samples were analyzed by TG and SEM to investigate the formation of carbon deposits. Figure 10 shows the DTG profile of each spent catalyst after DRM for 24 h of TOS. Ni@CeGdO₂ and Ni@CeSmO₂ exhibit an asymmetric peak at 604 °C with a shoulder at around 564–556 °C. The Ni@CeO₂ shows a broad and small peak at 503 °C and the Ni@CeZrO₂ catalyst does not show any peak in the TPO profile. According to the literature [6,48,58,59], the peak around 503 °C is ascribed to the oxidation of amorphous carbon, whereas the peak at 604 °C is due to the oxidation of carbon filaments with single or multiple walls. Table 4 presents the rate of carbon formation during the DRM for 24 h of TOS over the catalysts of our work and from the literature. Ni@CeGdO₂ has the highest carbon formation rate while no carbon formation is detected on Ni@CeZrO₂. High carbon formation was also observed over Cd and Sm-doped catalysts in the DRM reaction [60,61]. Taherian et al. [61] observed that the addition of Sm to SBA-15 induces the formation of carbon nanotubes over the support.

Table 4. Rate of carbon formation obtained by TGA in our work compared to the data obtained from literature.

Catalyst	Reaction Conditions	Rate of Carbon Formation (mgC·gcat ⁻¹ ·h ⁻¹)	Reference
Ni@CeO ₂	800 °C, CH ₄ :CO ₂ = 1:1	1.6	This work
Ni@CeGdO ₂	800 °C, CH ₄ :CO ₂ = 1:1	21.9	This work
Ni@CeSmO ₂	800 °C, CH ₄ :CO ₂ = 1:1	9.8	This work
Ni@CeZrO ₂	800 °C, CH ₄ :CO ₂ = 1:1	0.0	This work
Ni/CeO ₂	800 °C, CH ₄ :CO ₂ = 1:1	9.7	[6]
Ni/CeO ₂	700 °C, CH ₄ :CO ₂ = 1:1	0.4	[34]
Ni/CeZrO ₂ (75 wt% CeO ₂)	700 °C, CH ₄ :CO ₂ = 1:1	3.5	[34]
Ni/CeZrO ₂ (44 wt% CeO ₂)	700 °C, CH ₄ :CO ₂ = 1:1	1.7	[34]
Ni/CeZrO ₂ (28 wt% CeO ₂)	700 °C, CH ₄ :CO ₂ = 1:1	0.7	[34]
NiCu/Ce _{0.9} Gd _{0.1} O ₂	800 °C, CH ₄ :CO ₂ = 1:1	12.2	[60]
LaNiO ₃	800 °C, CH ₄ :CO ₂ = 1:1	27.0	[58]
LaNiO ₃ /SiCeO ₂	800 °C, CH ₄ :CO ₂ = 1:1	0.3	[58]
Ni/Gd-Y ₂ O ₃ (1% Gd)	700 °C, CH ₄ :CO ₂ = 1:1	17.0	[57]
Ni/Gd-Y ₂ O ₃ (2% Gd)	700 °C, CH ₄ :CO ₂ = 1:1	14.6	[57]
Ni/Gd-Y ₂ O ₃ (3% Gd)	700 °C, CH ₄ :CO ₂ = 1:1	11.8	[57]

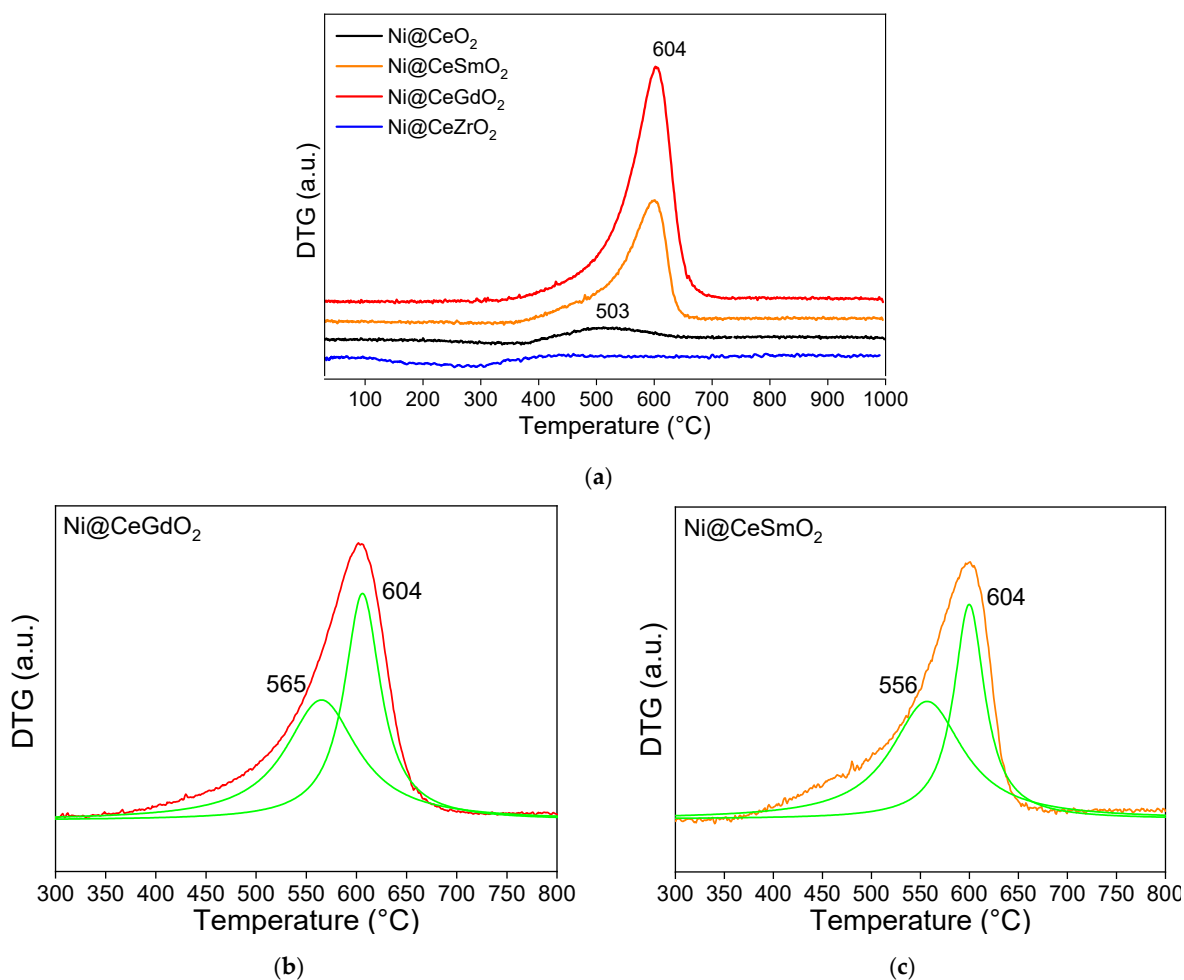


Figure 10. DTG profiles of (a) all used catalysts after DRM at 800 °C for 24 h of TOS with decomposition of the profiles for (b) Ni@CeGdO₂ and (c) Ni@CeSmO₂.

SEM images of the spent catalysts are shown in Figure 11. As observed by TGA, the Ni@CeGdO₂ and Ni@CeSmO₂ present a large formation of carbon filaments. Ni@CeO₂ catalyst also exhibits the presence of carbon filaments, but in a lower amount compared to Gd and Sm-doped catalysts. The SEM image of Ni@CeZrO₂ catalyst does not show carbon filaments, indicating that Zr doping suppresses the carbon deposition.

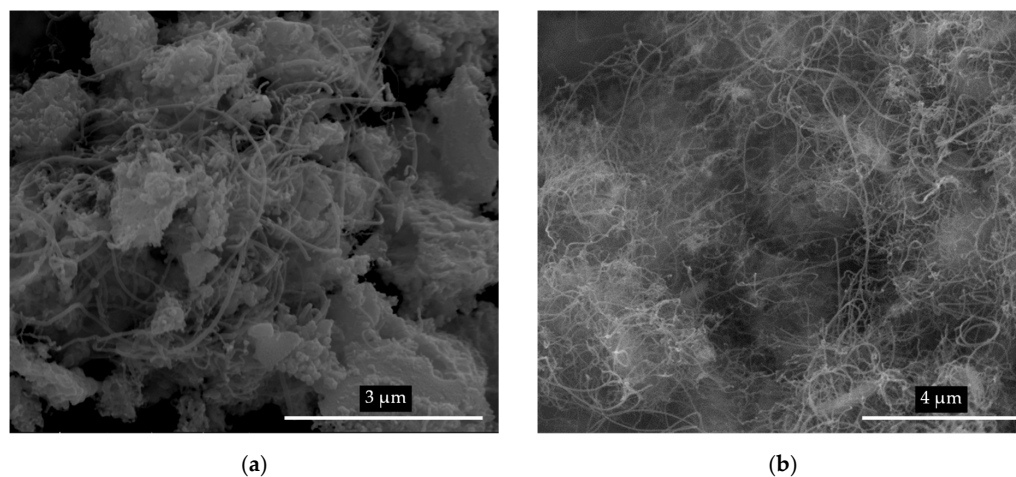


Figure 11. Cont.

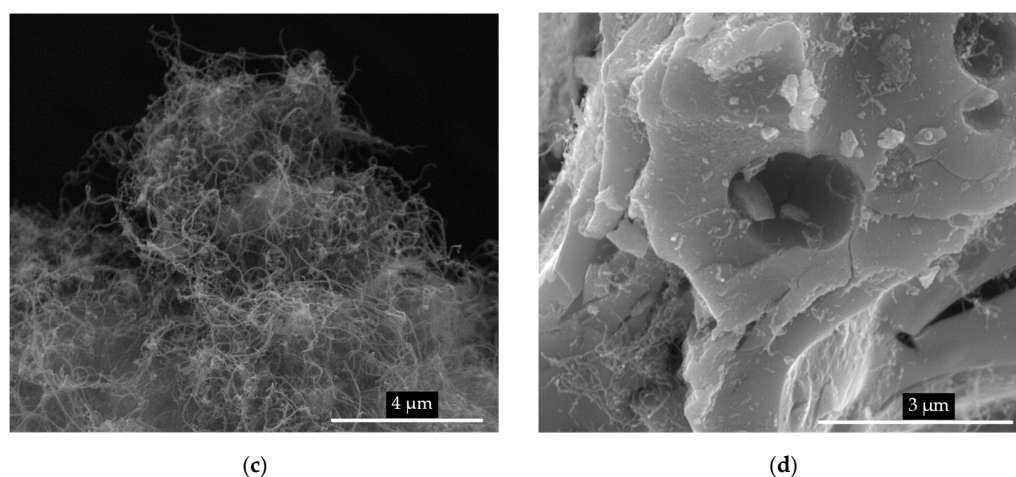


Figure 11. SEM images of spent catalysts after DRM at 800 °C for 24 h of TOS: (a) Ni@CeO₂, (b) Ni@CeGdO₂, (c) Ni@CeSmO₂ and (d) Ni@CeZrO₂.

3. Discussion

The mechanism of carbon formation during methane reforming reactions has been extensively studied in the literature [62–67]. According to these studies, the size of nickel particles plays an important role in the nucleation and growth of carbon filaments [48,68–72]. It has been reported that the formation of carbon is a structure sensitive reaction. The solubility of carbon through the metallic Ni particle is determined by its size; the larger the particle, the higher the driven force that promotes carbon diffusion. Recently, we investigated the relationship between the Ni particle size and the type and amount of carbon formed over Ni/CeO₂ catalysts in the DRM at 1073 K [48]. The results revealed that the Ni crystallite size affects the type and the rate of carbon formation during DRM. A maximum rate of carbon formation is achieved at around 20–30 nm. Below 10 nm and above 100 nm, the formation of carbon is negligible. Therefore, one of the strategies to suppress carbon formation during DRM reactions is to control the size of the metallic particle using different catalysts preparation methods. The support-embedded Ni approach to control Ni sintering is a promising alternative to design coke-resistant catalysts [9,11]. Such an approach avoids the addition of a second metallic site which can sometimes limit the Ni sintering [73,74]. Our previous work [6] demonstrated that controlling the Ni particle size by embedded process into CeO₂ support could decrease the rate of carbon formation during DRM reaction from 9.7 to 1.6 mgC·g_{cat}·h⁻¹.

In this work, Ni@CeO₂, Ni@CeGdO₂ and Ni@CeSmO₂ catalysts present Ni crystallite size between 9.5–11 nm, which favors the formation of carbon [75]. Ni@CeZrO₂ has Ni crystallite (5.7 nm) smaller than the critical size (below 10 nm), which inhibits carbon formation. The doping with Zr enhances CeO₂ thermal stability, which contributes to inhibit the growth of the Ni crystallite size during reduction in comparison to the other doped-ceria catalysts.

In spite of the importance of controlling the Ni particle to improve catalyst stability, several authors have reported the formation of carbon on Ni-based core-shell catalysts with high resistance to Ni sintering [12,76–79]. The presence of carbon species may be attributed to the absence of reducible support in the catalyst composition.

The support plays a key role in the CO₂ activation and carbon removal mechanism [23,24,80]. In the mechanism for DRM, the dissociation of methane on Ni surface produces hydrogen and highly reactive carbon species (C_α), which may follow two reaction pathways: (i) this carbon species reacts with oxygen from the support and the metal surface remains free of carbon deposits; or (ii) it polymerizes to less active carbon (C_β), then accumulates on the surface as amorphous carbon or dissolves into the Ni lattice, leading to the growth of carbon filaments. Supports with high oxygen mobility promote the oxidation of C_α species before their polymerization, forming CO, avoiding the accumulation of carbon

deposits. The release of oxygen from the support generates oxygen vacancies, in which CO_2 is preferentially dissociatively adsorbed as CO and O species, replenishing the oxygen vacancies of the support. Then, the support should have a high oxygen mobility to promote the removal of carbon formed during DRM conditions.

Ceria and ceria-mixed oxides have been largely used as a support to improve catalyst resistance to carbon formation in reforming reactions, especially DRM reaction [33,60,81]. Laosiripojana and Assabumrungrat [81] associated the high resistance to carbon formation observed for Ni supported on CeO_2 with high surface area to the higher oxygen mobility of this support, compared to Ni/ Al_2O_3 . For the DRM reaction, the reaction rate between the lattice oxygen from ceria with carbon deposits is improved and the carbon removal mechanism occurs successfully. In this case, the creation of oxygen vacancies is fundamental to promote the CO_2 dissociation and the oxygen mobility. Oxygen vacancies can be generated by the ceria reduction process or by the addition of dopants to the ceria lattice.

The addition of Gd, Sm, and Zr may create oxygen vacancies in the ceria structure, but their nature is different. Gd^{3+} and Sm^{3+} are trivalent cations and the partial substitution of Ce^{4+} by them creates oxygen vacancies by charge compensation [28]. The structure is not significantly affected because Gd^{3+} , Sm^{3+} , and Ce^{4+} have similar ionic radius (Gd^{3+} —1.16 Å; Sm^{3+} —1.08 Å; Ce^{4+} —0.97 Å). Different behavior occurs when Zr^{4+} is inserted, for which the charge is the same, but the ionic radii is smaller compared to Ce^{4+} (Zr^{4+} —0.84 Å). Therefore, the partial substitution of Zr^{4+} for Ce^{4+} creates oxygen vacancies due to the structural relaxation in the ceria structure [51,82]. Zr has a preference for six-fold coordination, in contrast to the eight-fold coordination observed in the fluorite structure [51]. The change in the structure directly affects the redox properties of ceria.

As observed in the in-situ XRD, TPR, and IOIE experiments, the addition of Zr allows the participation of oxygen atoms from bulk phase in the redox process, increasing the ceria reducibility over the material. The contraction in the lattice creates a driven force of oxygen bulk species to surface [37,51], increasing the number of oxygen species available to be released, which promotes the carbon removal mechanism in the DRM reaction. Oxygen isotopic exchange measurements show that a longer time is required for the exchange process, indicating the migration of oxygen bulk species to the surface [6,7].

In our work, the doping with Gd and Sm creates oxygen vacancies in the surface of the catalysts by charge compensation, quickly reaching the thermodynamic equilibrium for oxygen exchange. Moreover, the replacement of Ce^{4+} by non-reducible ions decreases the amount of reducible material on the catalyst. Therefore, the ceria reduction is not favored, resulting in a low ceria reducibility, as observed by TPR for Ni@CeGdO₂ and Ni@CeSmO₂ catalysts. The IOIE experiments show that the oxygen vacancies created on these materials are presented more pronounced over the surface, depressing bulk reduction.

Hennings and Reimert [49] evaluated the effect of Gd doped ceria with different concentrations and they observed that the addition of Gd into ceria structure could increase the dynamic oxygen exchange, but it suppresses the OSC value of the catalyst. According to the authors, the formation of vacancies by charge compensation hinders the formation of new vacancies by ceria reduction due to the presence of Gd^{3+} ions and lower Ce^{4+} conversion, leading to low ceria reducibility. Huang et al. [83] evaluated the influence of ceria doping with Sm (SDC) and Gd (GDC) in the DRM reaction. They observed that the GDC catalyst presented a higher density of the surface oxygen vacancies but lower oxygen-ion conductivity, which resulted in lower decoking activity compared to SDC catalyst. The authors attributed the negative effect on oxygen-ion conductivity to the stronger interaction between the oxygen vacancies and the surface O species.

Therefore, in our work, the doping with Gd and Sm reduces the redox cycle, since they have a combination of fewer oxygen atoms and lower ceria reducibility, resulting in a catalyst with high carbon formation compared to the undoped Ni@CeO₂. The Ni@CeZrO₂ catalyst presents higher ceria reducibility, as observed by TPR, leading to a high amount of bulk oxygen vacancies during the DRM reaction. The creation of bulk oxygen vacancies during the ceria reduction of Ni@CeZrO₂ promotes the oxygen-transport and, consequently,

the carbon gasification. Moreover, the CeZrO₂ solid solution stabilizes the Ni particle size at DRM condition, below the critical size of 10 nm.

4. Materials and Methods

4.1. Catalyst Preparation

The synthesis procedure is described in a previous work [6]. The solution with Ce(NO₃)₃ and the dopant precursor was prepared with a concentration of metals equal to 1.7 mol·L⁻¹ and Ce/dopant molar ratio of 4.0. The dopant precursors were Gd(NO₃)₃, Sm(NO₃)₃, and ZrO(NO₃)₂. To this solution, the appropriate amount of Ni(NO₃)₂ was added to obtain 10 wt% of Ni. Citric acid solution (6.7 mol·L⁻¹) was prepared in another beaker, with a citric acid/metals molar ratio equal to 1.0. Both solutions were mixed and maintained under stirring for 2 h at room temperature. After that, the sol-gel solution was heated up to 70 °C under vacuum (60 mmHg) to remove water and obtain the gel. The material was dried overnight at 100 °C and calcined in two steps: 300 °C for 2 h and 400 °C for 4 h, with a heating rate of 1 °C/min. The resulting catalysts were denominated as Ni@CeO₂, Ni@CeGdO₂, Ni@CeSmO₂, and Ni@CeZrO₂.

4.2. Characterization

4.2.1. X-ray Fluorescence

The composition of each catalyst was determined by X-ray fluorescence (XRF), using the RIGAKU RIX-3100 spectrometer. The samples were previously prepared as pellets.

4.2.2. N₂ Adsorption

The N₂ adsorption was used to measure the BET surface area of the reduced samples. The samples were reduced ex situ at 800 °C for 1 h under pure H₂ and passivated for 1 h under 5% O₂/N₂ at -70 °C. The N₂ adsorption was performed in an ASAP 2020 apparatus at -196 °C. The samples were previously degassed at 300 °C under vacuum.

4.2.3. In Situ X-ray Diffraction

The reduction of the samples was followed by in situ X-ray diffraction measurements (in situ XRD) in a Bruker D8 Advance X-ray Powder diffractometer. The apparatus was operated at 40 kV and 40 mA, using CoK_α radiation ($\lambda = 1.790307 \text{ \AA}$), equipped with $k\beta$ filter (Ni), a positive sensitive detector (VANTEC-1), and worked in scanning mode. All the data were corrected to Cu wavelength ($\lambda = 1.5406 \text{ \AA}$) using Bragg's law for comparison with the data from the literature. The samples were reduced under a 10 % H₂/He mixture (30 mL/min) from room temperature to 800 °C at 10 °C/min. The diffractograms were collected in the 2 θ range of 10–80°, using a scan rate of 0.05°/step and a scan time of 2 s/step at different temperatures: room temperature; 300, 500, and 800 °C.

4.2.4. Raman Spectroscopy

The RAMAN spectra were recorded at room temperature using a Horiba LabRam HR-UV800/Jobin-Yvon spectrometer equipped with a 532 nm wavelength laser.

4.2.5. Temperature-Programmed Reduction

Temperature-programmed reduction (TPR) was performed in an apparatus equipped with a thermal conductivity detector. The sample (300 mg) was previously oxidized at 400 °C for 1 h under air (30 mL/min). Then, the sample was cooled down to room temperature and heated under 10% H₂/Ar mixture (30 mL/min) from room temperature up to 1000 °C (10 °C/min).

4.2.6. ¹⁸O₂/¹⁶O₂ Isotopic Exchange

The experiments were carried out in a closed recycling system connected to a Pfeiffer Vacuum quadrupole mass spectrometer and a vacuum pumper. Hence, 20 mg of catalyst was pre-treated under ¹⁶O₂ flow (50 mL/min, 500 °C, 1 h) and evacuated for 1 h.

For the isothermal oxygen isotopic exchange (IOIE), the reaction occurred at 400 °C. It was inserted in the reactor 55 mbar of pure $^{18}\text{O}_2$ (≥ 99 at.%, ISOTEC) and each isotopomer concentration was analyzed by monitoring the following m/z signals: 32 ($^{16}\text{O}_2$), 34 ($^{18}\text{O}^{16}\text{O}$), 36 ($^{18}\text{O}_2$).

The following equations were used to calculate the amount of oxygen exchanged (N_e) and the atomic fraction of $^{18}\text{O}_2$ in the gas phase at the time t (α_g^t). N_g is the total number of oxygen atoms in the gas phase, w is the weight of catalyst, and α_g^0 is the initial atomic fraction of $^{18}\text{O}_2$ in the gas phase. Expressions for the calculation of α_g^t and N_e are given by Equations (1) and (2) respectively.

$$\alpha_g^t = \frac{\frac{1}{2}P_{34}^t + P_{36}^t}{P_{36}^t + P_{34}^t + P_{32}^t} \quad (1)$$

$$N_e = \left(\alpha_g^0 - \alpha_g^t\right) N_g \frac{1}{w} \quad (2)$$

4.3. Catalytic Test

The DRM reaction was carried out in a fixed-bed quartz reactor at atmospheric pressure. Prior to the reaction, the samples (20 mg of catalyst diluted with SiC: SiC/catalyst = 1.5) were reduced in situ under H_2 (30 mL/min) from room temperature to 800 °C (10 °C/min) for 1 h and purged with N_2 (30 mL/min) for 30 min. After this treatment, the reactant mixture with CH_4/CO_2 molar ratio of 1.0 at a flow rate of 100 mL/min was flowed through the catalyst for 24 h at 800 °C.

The reaction products were analyzed by gas chromatography (Agilent 6890) equipped with a thermal conductivity detector and Carboxen 1010 column (Supelco). The equations for CH_4 conversion (Equation (3)), CO_2 conversion (Equation (4)), and H_2/CO molar ratio (Equation (5)) are described below:

$$X_{\text{CH}_4} = \frac{(F_{\text{CH}_4})_{\text{in}} - (F_{\text{CH}_4})_{\text{out}}}{(F_{\text{CH}_4})_{\text{in}}} \times 100 \quad (3)$$

$$X_{\text{CO}_2} = \frac{(F_{\text{CO}_2})_{\text{in}} - (F_{\text{CO}_2})_{\text{out}}}{(F_{\text{CO}_2})_{\text{in}}} \times 100 \quad (4)$$

$$\frac{\text{H}_2}{\text{CO}} = \frac{(F_{\text{H}_2})_{\text{out}}}{(F_{\text{CO}})_{\text{out}}} \quad (5)$$

where F_{CH_4} , F_{CO_2} , F_{H_2} , and F_{CO} represent the molar flowrates of CH_4 , CO_2 , H_2 , and CO , respectively.

4.4. Carbon Analysis

4.4.1. Scanning Electron Microscopy

The post-reaction samples were analyzed using a field emission scanning electron microscope (SEM) (Quanta FEG 450 FEI). The microscope was operated with an accelerating voltage of 20 kV.

4.4.2. Thermogravimetric Analysis

The quantification of carbon deposits in the spent samples was performed by thermogravimetric analysis (TGA). The experiment was performed in a TA Instrument apparatus (SDT Q600) using 10 mg of sample. The sample was heated from 25 to 1000 °C at a heating rate of 10 °C/min under synthetic air (100 mL/min) while monitoring the weight variation.

5. Conclusions

The sol-gel method employed to synthesize Ni@CeO₂, Ni@CeGdO₂, Ni@CeSmO₂, and Ni@CeZrO₂ catalysts led to the formation of Ni nanoparticles embedded into ceria-doped oxide. The thermal stability of Zr avoids Ni metal sintering at high temperature (800 °C). Although the addition of dopants creates oxygen vacancies in the material, the ceria reducibility differs depending on the dopant used. The lattice distortions caused by Zr insertion in the ceria lattice enhance the bulk oxygen diffusion towards the surface, increasing ceria reducibility. The doping with Gd and Sm only creates oxygen vacancies by charge compensation, saturating the surface with oxygen vacancies and decreasing ceria reducibility in comparison to pure ceria and Zr-doped ceria. As a consequence, high carbon formation is detected for Sm and Gd-doped catalysts. Therefore, the combination of (i) small Ni crystallite size and (ii) high ceria reducibility promotes the balance between CH₄ decomposition and carbon gasification, resulting in the suppression of carbon deposits under DRM reaction and high activity for Ni@CeZrO₂ catalyst.

Author Contributions: Conceptualization, F.S.T., F.B.N. and N.B.; investigation, A.L.A.M.; writing—original draft preparation, A.L.A.M.; writing—review and editing, A.L.A.M., R.C.R.-N., F.E., F.S.T., F.B.N. and N.B.; supervision, F.S.T., F.B.N., F.E. and N.B.; project administration, F.B.N. and N.B.; funding acquisition, F.B.N. and N.B. All authors have read and agreed to the published version of the manuscript.

Funding: This research was funded by Coordenação de Aperfeiçoamento de Pessoal de Nível Superior (CAPES—Finance code 001; 88881.142911/2017-01), the Conselho Nacional de Desenvolvimento Científico e Tecnológico (CNPq—303667/2018-4; 305046/2015-2; 302469/2020-6; 310116/2019-82; CNPq-SisNANO—442604/2019-0), the Fundação de Amparo à Pesquisa do Estado do Rio de Janeiro (FAPERJ—26/010.253/2016; E-26/202.783/2017) and the Comité Français d’Évaluation de la Coopération Universitaire et Scientifique avec le Brésil (COFECUB—Ph-C 912/18) for scholarship and financial support.

Acknowledgments: Sandrine Arie and Nadia Guignard are gratefully acknowledged for in situ XRD and RAMAN experiments respectively. European Union (ERDF) and Région Nouvelle Aquitaine region are also gratefully acknowledged for their financial support. F.B.N. also thanks the French government through the Programme Investissement d’Avenir (I-SITE ULNE/ANR-16-IDEX-0004 ULNE) managed by the Agence Nationale de la Recherche, LIA CNRS France-Brazil “Energy & Environment”, Métropole Européenne de Lille (MEL) and Region Hauts-de-France for “CatBioInnov”.

Conflicts of Interest: The authors declare no conflict of interest.

References

1. González, M.O.A.; Gonçalves, J.S.; Vasconcelos, R.M. Sustainable Development: Case Study in the Implementation of Renewable Energy in Brazil. *J. Clean. Prod.* **2017**, *142*, 461–475. [[CrossRef](#)]
2. Ullah Khan, I.; Hafiz Dzarfan Othman, M.; Hashim, H.; Matsuura, T.; Ismail, A.F.; Rezaei-DashtArzhandi, M.; Wan Azelee, I. Biogas as a Renewable Energy Fuel—A Review of Biogas Upgrading, Utilisation and Storage. *Energy Convers. Manag.* **2017**, *150*, 277–294. [[CrossRef](#)]
3. Yang, L.; Ge, X.; Wan, C.; Yu, F.; Li, Y. Progress and Perspectives in Converting Biogas to Transportation Fuels. *Renew. Sustain. Energy Rev.* **2014**, *40*, 1133–1152. [[CrossRef](#)]
4. Yentekakis, I.V.; Panagiotopoulou, P.; Artemakis, G. A Review of Recent Efforts to Promote Dry Reforming of Methane (DRM) to Syngas Production via Bimetallic Catalyst Formulations. *Appl. Catal. B Environ.* **2021**, *296*, 120210. [[CrossRef](#)]
5. Shi, C.; Wang, S.; Ge, X.; Deng, S.; Chen, B.; Shen, J. A Review of Different Catalytic Systems for Dry Reforming of Methane: Conventional Catalysis-Alone and Plasma-Catalytic System. *J. CO₂ Util.* **2021**, *46*, 101462. [[CrossRef](#)]
6. Marinho, A.L.A.; Rabelo-Neto, R.C.; Epron, F.; Bion, N.; Toniolo, F.S.; Noronha, F.B. Embedded Ni Nanoparticles in CeZrO₂ as Stable Catalyst for Dry Reforming of Methane. *Appl. Catal. B Environ.* **2020**, *268*, 118387. [[CrossRef](#)]
7. Marinho, A.L.A.; Rabelo-Neto, R.C.; Epron, F.; Bion, N.; Noronha, F.B.; Toniolo, F.S. Pt Nanoparticles Embedded in CeO₂ and CeZrO₂ Catalysts for Biogas Upgrading: Investigation on Carbon Removal Mechanism by Oxygen Isotopic Exchange and DRIFTS. *J. CO₂ Util.* **2021**, *49*, 101572. [[CrossRef](#)]
8. Marinho, A.L.A.; Toniolo, F.S.; Noronha, F.B.; Epron, F.; Duprez, D.; Bion, N. Highly Active and Stable Ni Dispersed on Mesoporous CeO₂-Al₂O₃ Catalysts for Production of Syngas by Dry Reforming of Methane. *Appl. Catal. B Environ.* **2021**, *281*, 119459. [[CrossRef](#)]

9. Bian, Z.; Kawi, S. Sandwich-Like Silica@Ni@Silica Multicore-Shell Catalyst for the Low-Temperature Dry Reforming of Methane: Confinement Effect Against Carbon Formation. *ChemCatChem* **2018**, *10*, 320–328. [[CrossRef](#)]
10. Wang, F.; Xu, L.; Shi, W. Syngas Production from CO₂ Reforming with Methane over Core-Shell Ni@SiO₂ Catalysts. *J. CO₂ Util.* **2016**, *16*, 318–327. [[CrossRef](#)]
11. Pu, J.; Luo, Y.; Wang, N.; Bao, H.; Wang, X.; Qian, E.W. Ceria-Promoted Ni@Al₂O₃ Core-Shell Catalyst for Steam Reforming of Acetic Acid with Enhanced Activity and Coke Resistance. *Int. J. Hydrogen Energy* **2018**, *43*, 3142–3153. [[CrossRef](#)]
12. Zhang, J.; Li, F. Coke-Resistant Ni@SiO₂ Catalyst for Dry Reforming of Methane. *Appl. Catal. B Environ.* **2015**, *176–177*, 513–521. [[CrossRef](#)]
13. Ma, Y.; Ma, Y.; Li, J.; Ye, Z.; Hu, X.; Dong, D. Electrospun Nanofibrous Ni/LaAlO₃ Catalysts for Syngas Production by High Temperature Methane Partial Oxidation. *Int. J. Hydrogen Energy* **2022**, *47*, 3867–3875. [[CrossRef](#)]
14. Li, Z.; Mo, L.; Kathiraser, Y.; Kawi, S. Yolk-Satellite-Shell Structured Ni-Yolk@Ni@SiO₂ Nanocomposite: Superb Catalyst toward Methane CO₂ Reforming Reaction. *ACS Catal.* **2014**, *4*, 1526–1536. [[CrossRef](#)]
15. Han, J.W.; Kim, C.; Park, J.S.; Lee, H. Highly Coke-Resistant Ni Nanoparticle Catalysts with Minimal Sintering in Dry Reforming of Methane. *ChemSusChem* **2014**, *7*, 451–456. [[CrossRef](#)]
16. Charisiou, N.D.; Siakavelas, G.; Tzounis, L.; Sebastian, V.; Monzon, A.; Baker, M.A.; Hinder, S.J.; Polychronopoulou, K.; Yentekakis, I.V.; Goula, M.A. An in Depth Investigation of Deactivation through Carbon Formation during the Biogas Dry Reforming Reaction for Ni Supported on Modified with CeO₂ and La₂O₃ Zirconia Catalysts. *Int. J. Hydrogen Energy* **2018**, *43*, 18955–18976. [[CrossRef](#)]
17. Arora, S.; Prasad, R. An Overview on Dry Reforming of Methane: Strategies to Reduce Carbonaceous Deactivation of Catalysts. *RSC Adv.* **2016**, *6*, 108668–108688. [[CrossRef](#)]
18. Padi, S.P.; Shelly, L.; Komarala, E.P.; Schweke, D.; Hayun, S.; Rosen, B.A. Coke-Free Methane Dry Reforming over Nano-Sized NiO-CeO₂ Solid Solution after Exsolution. *Catal. Commun.* **2020**, *138*, 105951. [[CrossRef](#)]
19. Liu, Z.; Grinter, D.C.; Lustemberg, P.G.; Nguyen-Phan, T.D.; Zhou, Y.; Luo, S.; Waluyo, I.; Crumlin, E.J.; Stacchiola, D.J.; Zhou, J.; et al. Dry Reforming of Methane on a Highly-Active Ni-CeO₂ Catalyst: Effects of Metal-Support Interactions on C-H Bond Breaking. *Angew. Chem. Int. Ed. Engl.* **2016**, *55*, 7455–7459. [[CrossRef](#)]
20. Luisetto, I.; Tuti, S.; Romano, C.; Boaro, M.; Di Bartolomeo, E. Dry Reforming of Methane over Ni Supported on Doped CeO₂: New Insight on the Role of Dopants for CO₂ Activation. *J. CO₂ Util.* **2019**, *30*, 63–78. [[CrossRef](#)]
21. Löfberg, A.; Guerrero-Caballero, J.; Kane, T.; Rubbens, A.; Jalowiecki-Duhamel, L. Ni/CeO₂ Based Catalysts as Oxygen Vectors for the Chemical Looping Dry Reforming of Methane for Syngas Production. *Appl. Catal. B Environ.* **2017**, *212*, 159–174. [[CrossRef](#)]
22. Montini, T.; Melchionna, M.; Monai, M.; Fornasiero, P. Fundamentals and Catalytic Applications of CeO₂-Based Materials. *Chem. Rev.* **2016**, *116*, 5987–6041. [[CrossRef](#)]
23. Stagg-Williams, S.M.; Noronha, F.B.; Fendley, G.; Resasco, D.E. CO₂ Reforming of CH₄ over Pt/ZrO₂ Catalysts Promoted with La and Ce Oxides. *J. Catal.* **2000**, *194*, 240–249. [[CrossRef](#)]
24. Noronha, F.B.; Fendley, E.C.; Soares, R.R.; Alvarez, W.E.; Resasco, D.E. Correlation between Catalytic Activity and Support Reducibility in the CO₂ Reforming of Methane over Pt/CeZr_{1-x}O₂ Catalysts. *Chem. Eng. J.* **2001**, *82*, 21–31. [[CrossRef](#)]
25. Yao, H. Ceria in Automotive Exhaust Catalysts I. Oxygen Storage. *J. Catal.* **1984**, *86*, 254–265. [[CrossRef](#)]
26. Pérez-Coll, D.; Marrero-López, D.; Ruiz-Morales, J.C.; Núñez, P.; Abrantes, J.C.C.; Frade, J.R. Reducibility of Ce_{1-x}Gd_xO_{2-δ} in Prospective Working Conditions. *J. Power Sources* **2007**, *173*, 291–297. [[CrossRef](#)]
27. Aribi, K.; Soltani, Z.; Ghelamallah, M.; Granger, P. Structure, Morphology and Reducibility of Ceria-Doped Zirconia. *J. Mol. Struct.* **2018**, *1156*, 369–376. [[CrossRef](#)]
28. Mogensén, M.; Sammes, N.M.; Tompsett, G.A. Physical, Chemical and Electrochemical Properties of Pure and Doped Ceria. *Solid State Ion.* **2000**, *129*, 63–94. [[CrossRef](#)]
29. Fu, Y.-P.; Chen, S.-H.; Huang, J.-J. Preparation and Characterization of Ce_{0.8}M_{0.2}O_{2-δ} (M=Y, Gd, Sm, Nd, La) Solid Electrolyte Materials for Solid Oxide Fuel Cells. *Int. J. Hydrogen Energy* **2010**, *35*, 745–752. [[CrossRef](#)]
30. Nakajima, A.; Yoshihara, A.; Ishigame, M. Defect-Induced Raman Spectra in Doped CeO₂. *Phys. Rev. B* **1994**, *50*, 13297. [[CrossRef](#)] [[PubMed](#)]
31. Da Silva, A.A.A.; Bion, N.; Epron, F.; Baraka, S.; Fonseca, F.C.; Rabelo-Neto, R.C.; Mattos, L.V.; Noronha, F.B. Effect of the Type of Ceria Dopant on the Performance of Ni/CeO₂ SOFC Anode for Ethanol Internal Reforming. *Appl. Catal. B Environ.* **2017**, *206*, 626–641. [[CrossRef](#)]
32. Faria, E.C.; Neto, R.C.R.; Colman, R.C.; Noronha, F.B. Hydrogen Production through CO₂ Reforming of Methane over Ni/CeZrO₂/Al₂O₃ Catalysts. *Catal. Today* **2014**, *228*, 138–144. [[CrossRef](#)]
33. Kambolis, A.; Matralis, H.; Trovarelli, A.; Papadopoulou, C. Ni/CeO₂-ZrO₂ Catalysts for the Dry Reforming of Methane. *Appl. Catal. A Gen.* **2010**, *377*, 16–26. [[CrossRef](#)]
34. Zhang, F.; Liu, Z.; Chen, X.; Rui, N.; Betancourt, L.E.; Lin, L.; Xu, W.; Sun, C.; Abeykoon, A.M.M.; Rodriguez, J.A.; et al. Effects of Zr Doping into Ceria for the Dry Reforming of Methane over Ni/CeZrO₂ Catalysts: In Situ Studies with XRD, XAFS, and AP-XPS. *ACS Catal.* **2020**, *10*, 3274–3284. [[CrossRef](#)]
35. Hori, C.E.; Permana, H.; Ng, K.Y.S.; Brenner, A.; More, K.; Rahmoeller, K.M.; Belton, D. Thermal Stability of Oxygen Storage Properties in a Mixed CeO₂-ZrO₂ System. *Appl. Catal. B Environ.* **1998**, *16*, 105–117. [[CrossRef](#)]
36. Monte, R.D.; Kašpar, J. On the Role of Oxygen Storage in Three-Way Catalysis. *Top. Catal.* **2004**, *28*, 47–57. [[CrossRef](#)]

37. Rodriguez, J.A.; Hanson, J.C.; Kim, J.-Y.; Liu, G.; Iglesias-Juez, A.; Fernández-García, M. Properties of CeO₂ and Ce_{1-x}Zr_xO₂ Nanoparticles: X-Ray Absorption Near-Edge Spectroscopy, Density Functional, and Time-Resolved X-Ray Diffraction Studies. *J. Phys. Chem. B* **2003**, *107*, 3535–3543. [[CrossRef](#)]
38. Deguchi, H.; Yoshida, H.; Inagaki, T.; Horiuchi, M. EXAFS Study of Doped Ceria Using Multiple Data Set Fit. *Solid State Ion.* **2005**, *176*, 1817–1825. [[CrossRef](#)]
39. Durgasri, D.N.; Vinodkumar, T.; Reddy, B.M. Facile Synthesis of Catalytically Active CeO₂–Gd₂O₃ solid Solutions for Soot Oxidation. *J. Chem. Sci.* **2014**, *126*, 429–435. [[CrossRef](#)]
40. Karaca, T.; Altınçekiç, T.G.; Faruk Öksüzömer, M. Synthesis of Nanocrystalline Samarium-Doped CeO₂ (SDC) Powders as a Solid Electrolyte by Using a Simple Solvothermal Route. *Ceram. Int.* **2010**, *36*, 1101–1107. [[CrossRef](#)]
41. Da Fonseca, R.O.; Garrido, G.S.; Rabelo-Neto, R.C.; Silveira, E.B.; Simões, R.C.C.; Mattos, L.V.; Noronha, F.B. Study of the Effect of Gd-Doping Ceria on the Performance of Pt/GdCeO₂/Al₂O₃ Catalysts for the Dry Reforming of Methane. *Catal. Today* **2020**, *355*, 737–745. [[CrossRef](#)]
42. Bonk, A.; Remhof, A.; Maier, A.C.; Trottmann, M.; Schlupp, M.V.F.; Battaglia, C.; Vogt, U.F. Low-Temperature Reducibility of MxCe_{1-x}O₂ (M = Zr, Hf) under Hydrogen Atmosphere. *J. Phys. Chem. C* **2015**, *120*, 118–125. [[CrossRef](#)]
43. Mattos, L.V.; De Oliveira, E.R.; Resende, P.D.; Noronha, F.B.; Passos, F.B. Partial Oxidation of Methane on Pt/Ce–ZrO₂ Catalysts. *Catal. Today* **2002**, *77*, 245–256. [[CrossRef](#)]
44. Teles, C.A.; De Souza, P.M.; Braga, A.H.; Rabelo-Neto, R.C.; Teran, A.; Jacobs, G.; Resasco, D.E.; Noronha, F.B. The Role of Defect Sites and Oxophilicity of the Support on the Phenol Hydrodeoxygenation Reaction. *Appl. Catal. B Environ.* **2019**, *249*, 292–305. [[CrossRef](#)]
45. Taniguchi, T.; Watanabe, T.; Sugiyama, N.; Subramani, A.K.; Wagata, H.; Matsushita, N.; Yoshimura, M. Identifying Defects in Ceria-Based Nanocrystals by UV Resonance Raman Spectroscopy. *J. Phys. Chem. C* **2009**, *113*, 19789–19793. [[CrossRef](#)]
46. Siakavelas, G.I.; Charisiou, N.D.; Alkhoori, S.; Alkhoori, A.A.; Sebastian, V.; Hinder, S.J.; Baker, M.A.; Yentekakis, I.V.; Polychronopoulou, K.; Goula, M.A. Highly Selective and Stable Nickel Catalysts Supported on Ceria Promoted with Sm₂O₃, Pr₂O₃ and MgO for the CO₂ Methanation Reaction. *Appl. Catal. B: Environ.* **2021**, *282*, 119562. [[CrossRef](#)]
47. Loidant, S. Raman Spectroscopy as a Powerful Tool to Characterize Ceria-Based Catalysts. *Catal. Today* **2021**, *373*, 98–111. [[CrossRef](#)]
48. Da Fonseca, R.O.; Pongeggi, A.R.; Rabelo-Neto, R.C.; Simões, R.C.C.; Mattos, L.V.; Noronha, F.B. Controlling Carbon Formation over Ni/CeO₂ Catalyst for Dry Reforming of CH₄ by Tuning Ni Crystallite Size and Oxygen Vacancies of the Support. *J. CO₂ Util.* **2022**, *57*, 101880. [[CrossRef](#)]
49. Hennings, U.; Reimert, R. Investigation of the Structure and the Redox Behavior of Gadolinium Doped Ceria to Select a Suitable Composition for Use as Catalyst Support in the Steam Reforming of Natural Gas. *Appl. Catal. A Gen.* **2007**, *325*, 41–49. [[CrossRef](#)]
50. Bedrane, S.; Descorme, C.; Duprez, D. Investigation of the Oxygen Storage Process on Ceria- and Ceria–Zirconia-Supported Catalysts. *Catal. Today* **2002**, *75*, 401–405. [[CrossRef](#)]
51. Kuhn, M.; Bishop, S.R.; Rupp, J.L.M.; Tuller, H.L. Structural Characterization and Oxygen Nonstoichiometry of Ceria-Zirconia (Ce_{1-x}Zr_xO_{2-δ}) Solid Solutions. *Acta Mater.* **2013**, *61*, 4277–4288. [[CrossRef](#)]
52. Yentekakis, I.V.; Goula, G.; Hatzisymeon, M.; Betsi-Argyropoulou, I.; Botzolaki, G.; Kousi, K.; Kondarides, D.I.; Taylor, M.J.; Parlett, C.M.A.; Osatiashtiani, A.; et al. Effect of Support Oxygen Storage Capacity on the Catalytic Performance of Rh Nanoparticles for CO₂ Reforming of Methane. *Appl. Catal. B Environ.* **2019**, *243*, 490–501. [[CrossRef](#)]
53. Chen, J.; Wu, Q.; Zhang, J.; Zhang, J. Effect of Preparation Methods on Structure and Performance of Ni/Ce_{0.75}Zr_{0.25}O₂ Catalysts for CH₄–CO₂ Reforming. *Fuel* **2008**, *87*, 2901–2907. [[CrossRef](#)]
54. Ramírez-Cabrera, E.; Atkinson, A.; Chadwick, D. Reactivity of Ceria, Gd- and Nb-Doped Ceria to Methane. *Appl. Catal. B Environ.* **2002**, *36*, 193–206. [[CrossRef](#)]
55. Sadykov, V.A.; Yulia, V.F.; Alikina, G.M.; Lukashevich, A.I.; Muzykantov, V.S.; Rogov, V.A.; Moroz, E.M.; Zyuzin, D.A.; Ivanov, V.P.; Borchert, H.; et al. Mobility and Reactivity of Lattice Oxygen in Gd-Doped Ceria Promoted by Pt. *React. Kinet. Catal. Lett.* **2005**, *85*, 367–374. [[CrossRef](#)]
56. Wei, J.; Iglesia, E. Isotopic and Kinetic Assessment of the Mechanism of Reactions of CH₄ with CO₂ or H₂O to Form Synthesis Gas and Carbon on Nickel Catalysts. *J. Catal.* **2004**, *224*, 370–383. [[CrossRef](#)]
57. Al-Fatesh, A.S. Promotional Effect of Gd over Ni/Y₂O₃ Catalyst Used in Dry Reforming of CH₄ for H₂ Production. *Int. J. Hydrog. Energy* **2017**, *42*, 18805–18816. [[CrossRef](#)]
58. Rabelo-Neto, R.C.; Sales, H.B.E.; Inocência, C.V.M.; Varga, E.; Oszko, A.; Erdohelyi, A.; Noronha, F.B.; Mattos, L.V. CO₂ Reforming of Methane over Supported LaNiO₃ Perovskite-Type Oxides. *Appl. Catal. B Environ.* **2018**, *221*, 349–361. [[CrossRef](#)]
59. Kitiyanan, B.; Alvarez, W.E.; Harwell, J.H.; Resasco, D.E. Controlled Production of Single-Wall Carbon Nanotubes by Catalytic Decomposition of CO on Bimetallic Co–Mo Catalysts. *Chem. Phys. Lett.* **2000**, *317*, 497–503. [[CrossRef](#)]
60. Bonura, G.; Cannilla, C.; Frusteri, F. Ceria–Gadolinia Supported NiCu Catalyst: A Suitable System for Dry Reforming of Biogas to Feed a Solid Oxide Fuel Cell (SOFC). *Appl. Catal. B Environ.* **2012**, *121–122*, 135–147. [[CrossRef](#)]
61. Taherian, Z.; Yousefpour, M.; Tajally, M.; Khoshandam, B. Promotional Effect of Samarium on the Activity and Stability of Ni-SBA-15 Catalysts in Dry Reforming of Methane. *Microporous Mesoporous Mater.* **2017**, *251*, 9–18. [[CrossRef](#)]
62. Rostrup-Nielsen, J.; Trimm, D.L. Mechanisms of Carbon Formation on Nickel-Containing Catalysts. *J. Catal.* **1977**, *48*, 155–165. [[CrossRef](#)]

63. Rostrup-Nielsen, J. Equilibria of Decomposition Reactions of Carbon Monoxide and Methane over Nickel Catalysts. *J. Catal.* **1972**, *27*, 343–356. [[CrossRef](#)]
64. Kim, J.-H.; Suh, D.J.; Park, T.-J.; Kim, K.-L. Effect of Metal Particle Size on Coking during CO₂ Reforming of CH₄ over Ni–Alumina Aerogel Catalysts. *Appl. Catal. A Gen.* **2000**, *197*, 191–200. [[CrossRef](#)]
65. Rostrup-Nielsen, J. Coking on Nickel Catalysts for Steam Reforming of Hydrocarbons. *J. Catal.* **1974**, *33*, 184–201. [[CrossRef](#)]
66. Trimm, D.L. Coke Formation and Minimisation during Steam Reforming Reactions. *Catal. Today* **1997**, *37*, 233–238. [[CrossRef](#)]
67. Trimm, D.L. Catalysts for the Control of Coking during Steam Reforming. *Catal. Today* **1999**, *49*, 3–10. [[CrossRef](#)]
68. Rostrup-Nielsen, J.R.; Sehested, J.; Nørskov, J.K. Hydrogen and Synthesis Gas by Steam- and CO₂ Reforming. In *Advances in Catalysis*; Academic Press: Cambridge, MA, USA, 2002; Volume 47, pp. 65–139. ISBN 0360-0564.
69. Bengaard, H.S.; Nørskov, J.K.; Sehested, J.; Clausen, B.S.; Nielsen, L.P.; Molenbroek, A.M.; Rostrup-Nielsen, J.R. Steam Reforming and Graphite Formation on Ni Catalysts. *J. Catal.* **2002**, *209*, 365–384. [[CrossRef](#)]
70. Toebe, M.L.; Bitter, J.H.; Van Dillen, A.J.; De Jong, K.P. Impact of the Structure and Reactivity of Nickel Particles on the Catalytic Growth of Carbon Nanofibers. *Catal. Today* **2002**, *76*, 33–42. [[CrossRef](#)]
71. Chen, D.; Christensen, K.O.; Ochoa-Fernández, E.; Yu, Z.; Tøtdal, B.; Latorre, N.; Monzón, A.; Holmen, A. Synthesis of Carbon Nanofibers: Effects of Ni Crystal Size during Methane Decomposition. *J. Catal.* **2005**, *229*, 82–96. [[CrossRef](#)]
72. Vogt, C.; Kranenborg, J.; Monai, M.; Weckhuysen, B.M. Structure Sensitivity in Steam and Dry Methane Reforming over Nickel: Activity and Carbon Formation. *ACS Catal.* **2020**, *10*, 1428–1438. [[CrossRef](#)]
73. Wang, C.; Su, T.; Qin, Z.; Ji, H. Coke-Resistant Ni-Based Bimetallic Catalysts for the Dry Reforming of Methane: Effects of Indium on the Ni/Al₂O₃ Catalyst. *Catal. Sci. Technol.* **2022**, *12*, 4826–4836. [[CrossRef](#)]
74. Yan, N. Ni-Ir/MgAl₂O₄ for Balanced Carbon Deposition-Elimination in Methane Dry Reforming. *Chem Catal.* **2022**, *2*, 1520–1521. [[CrossRef](#)]
75. Lercher, J.A.; Bitter, J.H.; Hally, W.; Niessen, W.; Seshan, K. Design of Stable Catalysts for Methane–Carbon Dioxide Reforming. In *Studies in Surface Science and Catalysis, Proceedings of the 11th International Congress On Catalysis—40th Anniversary, Baltimore, MD, USA, 30 June–5 July 1996*; Hightower, J.W., Nicholas Delgass, W., Iglesia, E., Bell, A.T., Eds.; Elsevier: Amsterdam, The Netherlands, 1996; Volume 101, pp. 463–472.
76. Baktash, E.; Littlewood, P.; Schomäcker, R.; Thomas, A.; Stair, P.C. Alumina Coated Nickel Nanoparticles as a Highly Active Catalyst for Dry Reforming of Methane. *Appl. Catal. B Environ.* **2015**, *179*, 122–127. [[CrossRef](#)]
77. Han, B.; Wang, F.; Zhang, L.; Wang, Y.; Fan, W.; Xu, L.; Yu, H.; Li, Z. Syngas Production from Methane Steam Reforming and Dry Reforming Reactions over Sintering-Resistant Ni@SiO₂ Catalyst. *Res. Chem. Intermed.* **2019**, *46*, 1735–1748. [[CrossRef](#)]
78. Huang, Q.; Fang, X.; Cheng, Q.; Li, Q.; Xu, X.; Xu, L.; Liu, W.; Gao, Z.; Zhou, W.; Wang, X. Synthesis of a Highly Active and Stable Nickel-Embedded Alumina Catalyst for Methane Dry Reforming: On the Confinement Effects of Alumina Shells for Nickel Nanoparticles. *ChemCatChem* **2017**, *9*, 3563–3571. [[CrossRef](#)]
79. Zhang, L.; Wang, F.; Zhu, J.; Han, B.; Fan, W.; Zhao, L.; Cai, W.; Li, Z.; Xu, L.; Yu, H.; et al. CO₂ Reforming with Methane Reaction over Ni@SiO₂ Catalysts Coupled by Size Effect and Metal-Support Interaction. *Fuel* **2019**, *256*, 115954. [[CrossRef](#)]
80. Ross, J.R.H.; Van Keulen, A.N.J.; Hegarty, M.E.S.; Seshan, K. The Catalytic Conversion of Natural Gas to Useful Products. *Catal. Today* **1996**, *30*, 193–199. [[CrossRef](#)]
81. Laosiripojana, N.; Assabumrungrat, S. Catalytic Dry Reforming of Methane over High Surface Area Ceria. *Appl. Catal. B Environ.* **2005**, *60*, 107–116. [[CrossRef](#)]
82. Vlaic, G.; Fornasiero, P.; Geremia, S.; Kašpar, J.; Graziani, M. Relationship between the Zirconia-Promoted Reduction in the Rh-Loaded Ce_{0.5}Zr_{0.5}O₂ Mixed Oxide and the Zr–O Local Structure. *J. Catal.* **1997**, *168*, 386–392. [[CrossRef](#)]
83. Huang, T.-J.; Lin, H.-J.; Yu, T.-C. A Comparison of Oxygen-Vacancy Effect on Activity Behaviors of Carbon Dioxide and Steam Reforming of Methane over Supported Nickel Catalysts. *Catal. Lett.* **2005**, *105*, 239–247. [[CrossRef](#)]